Available online at www.sciencedirect.com
ScienceDirect
International Journal of Heat and Mass Transfer 51 (2008) 1003–1016
International Journal of HEAT and MASS TRANSFER
www.elsevier.com/locate/ijhmt

Numerical and experimental investigation of two phase flow during boiling in a coiled tube

Z. Yang, X.F. Peng *, P. Ye

Laboratory of Phase Change and Interfacial Transport Phenomena, Department of Thermal Engineering, Tsinghua University, Beijing 100084, China

Received 19 September 2006; received in revised form 11 January 2007
Available online 21 August 2007

Abstract

A numerical simulation, using the VOF multiphase flow model, and the corresponding experiments were conducted to investigate the boiling flow of R141B in a horizontal coiled tube. The numerical predictions of phase evolution were in a good agreement with the experimental observations, and the two phase flow in the tube bends was much more complicated due to the influence of liquid–vapor interaction with the interface evolution. The associated heat transfer was also considered. It was found that the temperature profile in the two phase flow was significantly affected by the phase distribution and higher temperature always appears in the vapor region.
© 2007 Elsevier Ltd. All rights reserved.

Keywords: Boiling flow; Coiled tube; Phase distribution; Flow pattern; Numerical simulation; VOF

1. Introduction

Tube/channel evaporators are widely employed in various energy systems, like HVACR and petrochemical industries. As well-known, both associated flow boiling and two phase flow play very important roles in evaporators and are still far from being fully understood. As a result, present evaporators are normally designed with a profuse safety factor, resulting in an unnecessary tube length and high superheat of vapor at the exit. Further understanding of flow boiling could potentially decrease the manufacture cost and energy consumption, and furthermore obtain better performance.

Flow boiling and associated two phase flow in tubes/channels was comprehensively investigated as a classical topic of boiling heat transfer in open literature. Particularly, numerous investigations were conducted for horizontal, adiabatic gas–liquid two-phase flow in tubes [1]. Two-phase flow with phase change is very complicated. In addition to inertia, viscous and pressure forces present in single-phase flow, two-phase flows are greatly affected by interfacial tension forces, the wetting characteristics of the liquid on the tube wall and the exchange of momentum between the liquid and vapor phases in the flow, also by phase distribution, mass exchange among two phases, flow pattern evolution and phase redistribution if with phase change. Usually, traditional liquid–gas flow modes in a horizontal tube includes bubbly flow, plug flow, slug flow, wavy flow and annular flow, and also stratified flow, stratified/wavy flow, intermittent flow, mist flow and so on. Theofanous and Hanratty [2] presented an overview of flow modes of steady, fully developed multifluid flows in tubes/channels. Depending on operating conditions and fluid properties, most of these flow modes are also expected to occur in the two-phase flow systems with phase change of evaporation.

Normally flow pattern maps obtained from experiments are employed to describe two phase flow, like vapor–liquid flow configurations, and boiling heat transfer in tubes/channels. The flow pattern map proposed by Taitel and Dukler [1] is widely applied for adiabatic two-phase flow, which identified the flow mode as a function of Martinelli parameter X_{tt}. Later, Hashizume [3] found that the boundaries or

* Corresponding author. Tel./fax: +86 10 6278 9751.
E-mail address: pxf-dte@mail.tsinghua.edu.cn (X.F. Peng).

0017-9310/$ - see front matter © 2007 Elsevier Ltd. All rights reserved.
doi:10.1016/j.ijheatmasstransfer.2007.05.025

Nomenclature

$C_{v,l}$	heat capacity under constant volume of the liquid (J kg^{-1} K^{-1})
$C_{v,v}$	heat capacity under constant volume of the vapor (J kg^{-1} K^{-1})
E	apparent energy with the zero defined at 298.15 K (J/kg)
F_{vol}	the interface-induced volumetric force (N/m^3)
g	gravity acceleration, 9.81 m s^{-2}
h_{LH}	latent heat at 298.15 K (J kg^{-1})
I	3 × 3 unit tensor
k	thermal conductivity (W m^{-1} K^{-1})
p	pressure (Pa)
Δp	pressure drop between the inlet and outlet (Pa)
Δp_m	time-averaged Δp (Pa)
Q	heat source term due to phase change at 298.15 K (W/m^3)
S	mass source term due to phase change (kg s^{-1} m^{-3})
T	temperature (K)
t	time (s)
$\vec{v}$	velocity vector (m/s)
v	magnitude of $\vec{v}$ (m/s)

Greek symbols

α_l	volume fraction of liquid phase (–)
α_v	volume fraction of vapor phase (–)
$\alpha_{v,out}$	area-averaged vapor volume fraction at the outlet (–)
$\alpha_{v,out,m}$	time-averaged $\alpha_{v,out}$ (–)
μ	viscosity (kg m^{-1} s^{-1})
ρ	density (kg m^{-3})

Subscripts

l	liquid
v	vapor
sat	saturation

transitions of flow pattern in the flow pattern map for boiling two-phase flows of a refrigerant differs significantly from those presented in adiabatic two-phase flow. Actually, for flow boiling, mass transfer plays an important role in the dynamic phase distribution and hence flow mode. The adiabatic flow pattern maps, such as Baker map or Taitel and Dukler map, showed very poor accuracy of prediction of flow mode in various cases, even for diabatic two-phase flows. Based on Taitel and Dukler map, Steiner [4] developed a diabatic flow pattern map based on R-12 and R-22 data. Recently, Kattan et al. [5–7] modified the axes of the map to improve Steiner map for two phase flows with evaporation, and accounted for the influences of heat flux and dryout on the flow mode transition. This work was based on R-134a, R-123, R-402A and R-404A data under evaporating conditions and could be applied to both diabatic and adiabatic two-phase flows. They also proposed a new flow boiling model based on local flow patterns. Thome and Hajal [8] presented a simpler method to obtain the equivalent results of Kattan map. The newest version of Kattan map was proposed by Wojtan [9], which considered dynamic void fraction and cross-sectional locus of the liquid–vapor interface, and the effects of heat flux on the transition to mist flow.

In last decade numerical simulations are increasingly and widely employed to investigate two phase flow during flow boiling in tubes/channels. Recently, a series of so-called "one-fluid" methods was proposed to correctly advent the phase boundary in a number of adiabatic problems, like volume-of-fluid (VOF) [10], CIP [11], the level-set [12,13], and phase field [14] methods. For problems involving phase-change, the energy equation should be considered to account for the heat absorption/release during evaporation/condensation and the volume change as well. Proper source terms should be added in the governing equations to model the phase-change phenomenon [15–17].

Coiled tubes is a kind of very important tube type for industrial applications. However, except for the case of single phase flow, very limited experimental investigations and theoretical/numerical analyses have been found in the open literature to understand the two phase and heat transfer during boiling in coiled tubes. Wu et al. [18] applied the Eulerian multiphase flow model to investigate the boiling process in a coiled tube and paid special interests in flow mode. They found that the phase distributions showed a continuous stratification in the horizontal tubes and were influenced by both buoyancy force and centrifugal force in the tube bends. Although a gradually increase of vapor volume along the flow was shown in their work, the most interesting flow details, such as flow mode and bubble motion, were not presented.

In the present paper, an attempt was made to combine the experimental observation with numerical simulation to explore and understand fundamentals of two-phase flow behavior during flow boiling in coiled tubes. Numerical simulations were conducted for flow boiling in a horizontal coiled tube using refrigerant R-141B as the work fluid. Special interests were addressed on the flow mode evolution and exploring the details of local flow and transport phenomena. Meanwhile, an experiment was conducted to validate the simulations.

2. Simulation

2.1. Basic considerations

The modeling of boiling flow was accomplished by using volume of fluid model (VOF) in CFD software Fluent 6.0

(USA), with a user defined function (UDF) as an evaporation model. In VOF model, volume fractions of each phase in a computational cell are recorded, and volume fractions of all phases sum to unity.

$$\alpha_l + \alpha_v = 1 \tag{1}$$

Information on phase distribution can be directly extracted from the volume fractions. For instance, the computational grid is empty or full of the liquid when α_l reaches the minimum value of zero or the maximum value of unit, and contains phase interface with α_l between 0 and 1.

The tracking of the interface between phases was accomplished by solving continuity equations for the volume fractions of different phases. For the liquid and vapor phases, the equations are:

$$\frac{\partial \alpha_l}{\partial t} + \nabla \cdot (\vec{v}\,\alpha_l) = -\frac{S}{\rho_l} \tag{2a}$$

$$\frac{\partial \alpha_v}{\partial t} + \nabla \cdot (\vec{v}\,\alpha_v) = \frac{S}{\rho_v} \tag{2b}$$

The continuity, momentum and energy equations are, respectively,

$$\frac{\partial(\rho\,\vec{v})}{\partial t} + \nabla \cdot (\rho\,\vec{v}\,\vec{v}) \tag{3}$$

$$= -\nabla p + \nabla \cdot \left[\mu(\nabla\,\vec{v} + \nabla\vec{v}^{\mathrm{T}}) - \frac{2}{3}\mu\nabla \cdot \vec{v}\, I\right] + \rho\vec{g} + F_{\mathrm{vol}} \tag{4}$$

$$\frac{\partial(\rho E)}{\partial t} + \nabla \cdot [\vec{v}(\rho E + p)] = \nabla \cdot (k\nabla T) + Q \tag{5}$$

where

$$\rho = \alpha_l\rho_l + \alpha_v\rho_v \tag{6}$$

$$k = \alpha_l k_l + \alpha_v k_v \tag{7}$$

$$\mu = \alpha_l\mu_l + \alpha_v\mu_v \tag{8}$$

$$E = \frac{\alpha_l\rho_l E_l + \alpha_v\rho_v E_v}{\alpha_l\rho_l + \alpha_v\rho_v} \tag{9}$$

$$E_l = C_{v,l}(T - 298.15), \quad E_v = C_{v,v}(T - 298.15) \tag{10}$$

The accuracy of the temperature near the interface is considerably corrupt in cases where large temperature differences exist between the phases. Such problems also arise in cases where the properties vary by several orders of magnitude. For example, if a model includes liquid metal in combination with air, the conductivities of the materials can have difference as much as four orders of magnitude. Such large discrepancies in properties lead to equation sets with anisotropic coefficients, which can consequently lead to the issues of convergence and precision.

In FLUENT, a formulation of the continuum surface force (CSF) model is used, and the surface tension can finally be written in terms of the pressure jump across the surface. The force at the surface can be expressed as a volume force F_{vol}, using the divergence theorem. The volume force acts as the source term in the momentum equation and has the following form:

$$F_{\mathrm{vol}} = \sigma_{lv}\frac{\alpha_l\rho_l\kappa_v\nabla\alpha_v + \alpha_v\rho_v\kappa_l\nabla\alpha_l}{0.5(\rho_l + \rho_v)} \tag{11}$$

where σ_{lv} is the interfacial tension between the liquid and vapor. The curvatures of liquid and vapor are defined as

$$\kappa_l = \frac{\Delta\alpha_l}{|\nabla\alpha_l|}, \quad \kappa_v = \frac{\Delta\alpha_v}{|\nabla\alpha_v|} \tag{12}$$

The geometric reconstruction scheme represents the interface between fluids using a piecewise-linear approach. In FLUENT this scheme is the most accurate and is applicable for general unstructured meshes.

In this simulation, the realizable k–ε model [19] was adopted, and particularly its substantial improvements over the standard k–ε model where the flow features include strong streamline curvature, vortices, and rotation [19,20].

The pressure-implicit with splitting of operators (PISO) pressure–velocity coupling scheme, part of the SIMPLE family of algorithms, is based on the higher degree of the approximate relation between the corrections for pressure and velocity. Compared with the SIMPLE and SIMPLEC algorithms, the PISO algorithm performs two additional corrections: neighbor correction and skewness correction. These corrections help to improve the efficiency of calculation. These were considered in the present simulations. Upwind scheme of second order accuracy was adopted to discretize the momentum and energy equations. The simulation test indicates that a good convergence was reached if the under-relaxation factors were used at values: 0.3 (pressure), 1 (density), 1 (body force), 0.7 (momentum), volume fraction (0.2) and 1 (energy).

2.2. Transport description

2.2.1. Mass transfer

Lee [21] developed a mass transfer model concerning the process of evaporating and condensing. In their model, phase change was assumed to occur at a constant pressure and at a quasi thermo-equilibrium state, and the mass transfer was mainly dependent of the saturate temperature. Lee's model was herein applied to consider phase change process here, or described as

$$\begin{aligned} S &= r_l\alpha_l\rho_l(T_l - T_{\mathrm{sat}})/T_{\mathrm{sat}} \quad T_l \geqslant T_{\mathrm{sat}} \\ &= r_v\alpha_v\rho_v(T_l - T_{\mathrm{sat}})/T_{\mathrm{sat}} \quad T_l < T_{\mathrm{sat}} \end{aligned} \tag{13}$$

In this investigation, the interfacial temperature was assumed at the saturation temperature. For this purpose, the coefficients r_l and r_v were hereby specified at $100\ \mathrm{s}^{-1}$ in order to numerically maintain the interface temperature within $T_{\mathrm{sat}} \pm 1$ K. Excessively large values of r_l andr_v cause a numerical convergence problem, while too small values lead to a significant deviation between the interfacial temperature and the saturation temperature.

2.2.2. Heat transfer

The heat transfer was simply determined from the mass rate of evaporation or condensation, in addition to the conduction and convection. As long as the mass transfer was obtained, the heat transfer could be directly determined as

$$Q = -h_{LH}S \tag{14}$$

2.3. Geometrical configuration

The computational domain is strictly the same as the coiled tube employed in the experiment. Corresponding to the designed test section consisting of six straight tubes and five bend sections, the computation domain and boundaries are illustrated in Fig. 1. The parameters characterizing the tube geometry are listed in Table 1. The computational mesh of the tube volume was comprised by 118,800 hexahedral girds, and the grid number on the cross-section area of the tube was 135.

3. Experiment

To validate the numerical simulations, an experimental investigation was also conducted to visually observe the fundamental phenomena of the flow boiling and associated two-phase flow in the coiled tube. The experimental facility employed is shown in Fig. 2 and the test section was installed horizontally. The working fluid, R141B, was circulated in a closed loop, consisting of a liquid tank, pump, flow meter, pre-heater, pre-mixing chamber, test section, post-mixing chamber, filter and condenser. The flow pattern in the transparent test section was recorded by a high-speed CCD video system (at a speed of 500 fps or much higher speeds, dependent upon the experimental conditions) and transferred to a computer for further analysis or comparison with the simulation.

The test section, shown in Fig. 1c, was a coiled tube made of quartz glass, which is high temperature durable, low thermal expansion and highly transparent. The inner diameter of the tube was 6 mm and the tube wall thickness was 1 mm. The surface of the tube is coated with an electric conducting metal oxide film through which alternating current was applied to heat the tube. The heating power was adjusted by changing the voltage applied on the two copper electrodes at the ends of the tube. The physical properties of R141B are listed in Table 2.

Table 1
Geometrical parameters of the coiled tube

d/mm	l_1/mm	l_2/mm
6	28	70

The flowrate, heating AC voltage and electric resistance were measured with accuracies of ±2%, ±2.7% and ±0.7%, respectively. The spatial resolution of CCD image was 512 pixels for 148 mm, so the maximum spatial error of the image should be no more than one or several pixels, depending on the image quality. Here, a conservative value of ±0.5 mm can be safely adopted as the deviation of image resolution.

4. Flow behavior

4.1. Flow patterns

The complete development of flow mode in a straight heating tube mainly consists of six different regimes, namely bubbly, churn, slug, stratified, annular and mist flow. Under proper working conditions, e.g. flowrate, heat flux, inlet liquid temperature and pressure, these flow modes can be observed in both simulations and experiments conducted for a coiled tube. In this investigation, six working conditions were investigated both numerically and experimentally, see the details in Table 3. Two flowrates and three heat fluxes were selected to comprise six working conditions according to the industrial interests (required by Advanced Heat Transfer LLC, USA). Both simulations and experiments were strictly subject to these conditions.

The simulated flow patterns are compared with typical experimental photos, as shown in Fig. 3. Note that in cases 2, 3 and 5, due to some technical problems, only regional photos of the first bend were recorded during the experiments. However, the downstream flow pattern was observed to be similar to that in case 6.

Generally, the flow patterns numerically predicted are in a good agreement with the experimental observations in all

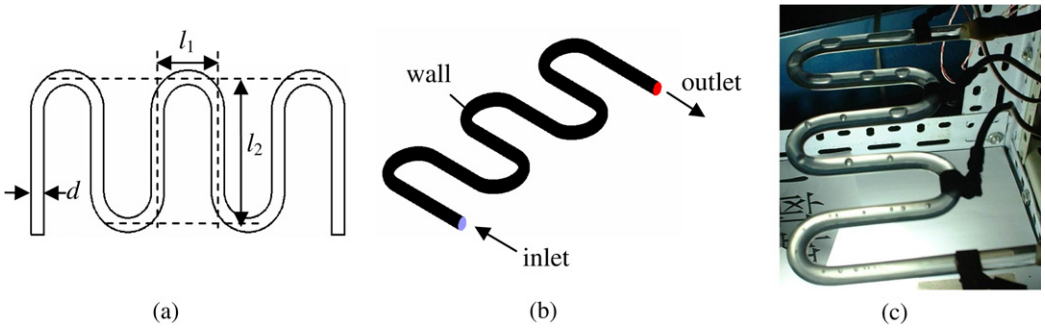

Fig. 1. Coiled tube: (a) geometry; (b) computational domain; (c) test section.

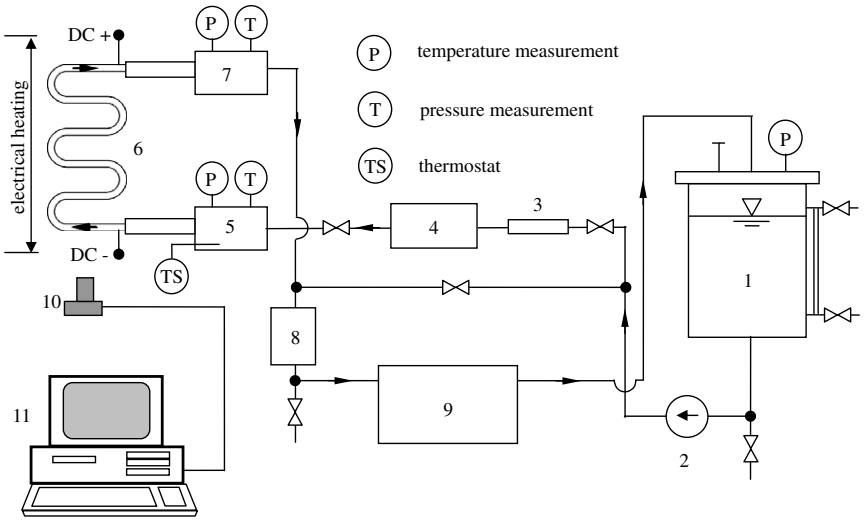

1. tank; 2. pump; 3. flow meter; 4. pre-heater; 5. pre-mixing chamber; 6. test section; 7. post-mixing chamber; 8. filter; 9. condenser; 10. CCD; 11. computer

Fig. 2. Test facility.

Table 2
Properties of R141B at $P = 0.102$ MPa and $T_{sat} = 307.65$ K

Liquid		Vapor	
k_l/(W m^{-1} K^{-1})	0.09204	k_v/(W m^{-1} K^{-1})	0.00998
$C_{v,l}$/(J kg^{-1} K^{-1})	1165	$C_{v,v}$/(J kg^{-1} K^{-1})	793.5
h_l/(J/kg)	2.366×10^5	h_v/(J/kg)	4.604×10^5
ρ_l/(kg/m^3)	1220	ρ_v/(kg/m^3)	4.867
μ_l/(kg m^{-1} s^{-1})	378.2	μ_v/(kg m^{-1} s^{-1})	9.481

Table 3
Cases in both simulations and experiments

	q''/(W/m^2)	Q/(l/h)	Subcooled/K
Case 1	6888	10	8.5
Case 2	17,848	10	8.5
Case 3	24,874	10	8.5
Case 4	6888	15	10.5
Case 5	17,848	15	8.5
Case 6	24,874	15	8.5

cases. Bubbly flow (denoted as 0–1 in the illustrations) appeared in all cases, especially in cases 1 and 4 whose heat fluxes were the lowest in the experiments. In the entrance region of the coiled tube, the fluid is subcooled, and the applied heat amount mainly contributes to raise the fluid temperature. Either decreasing wall heat flux or increasing the mass flowrate would extend the bubbly flow region significantly, as shown in cases 1 and 4. Contrarily, the smallest flowrate and the highest heat flux lead to the shortest bubbly flow region, as shown in case 3. Along the flow direction, small bubbles, absorbing vapor or coalescing with other bubbles, continuously grow up, and the flow gradually changes into a churn type. The simulation shows that the longest churn region occurs in case 4 where the flowrate is the largest while the heat flux is the smallest. Such a working condition favors a slow growth of bubbles. The shortest churn region appears in case 3 due to the rapid evaporation on the liquid–vapor interface. Slug flow was both experimentally observed and numerically predicted for all the cases except case 4, as shown in Fig. 3. Case 1 exhibits a typical slug flow region because the wall heat flux in this case is small and a relatively long flow distance is needed for the fluid to absorb the amount of energy enough for the transition from slug flow into stratified flow. In case 4, the flow mode does not develop into slug flow before exiting the tube. However, if the tube is long enough, the longest slug flow region should be expected. Stratified flow was also observed and predicted for all the cases but case 4. When several slug bubbles coalesce, the flow turns into a stratified one, liquid phase flowing along the lower part of channel and vapor phase along the upper part due to the gravity. After the stratified mode, the flow turns into a wavy type, as observed in the experiments. The fluid is further accelerated due to liquid vaporization, meanwhile the strong viscous shearing causes the vapor–liquid interface drastically waving. Not exactly as in the experiments, the wavy flow does not developed well in the simulation. The computed waving thin liquid layer tends to break into liquid patches rather than maintain a continuous film on the tube surface. Further study shows that the coarse grid configuration is mainly responsible for the broken thin liquid film. When the film is thinner than the thickness of one grid, flow fluctuation is easy to break the film into separate liquid patches, as shown in Fig. 4b. Fig. 4a shows the simulated liquid patches on the rear straight tube wall in case 5, while the corresponding experimental observation in Fig. 4c showed a continuous thin film on the tube wall. It can be expected that the thin film flow can be properly modeled if the grids near wall are sufficiently good.

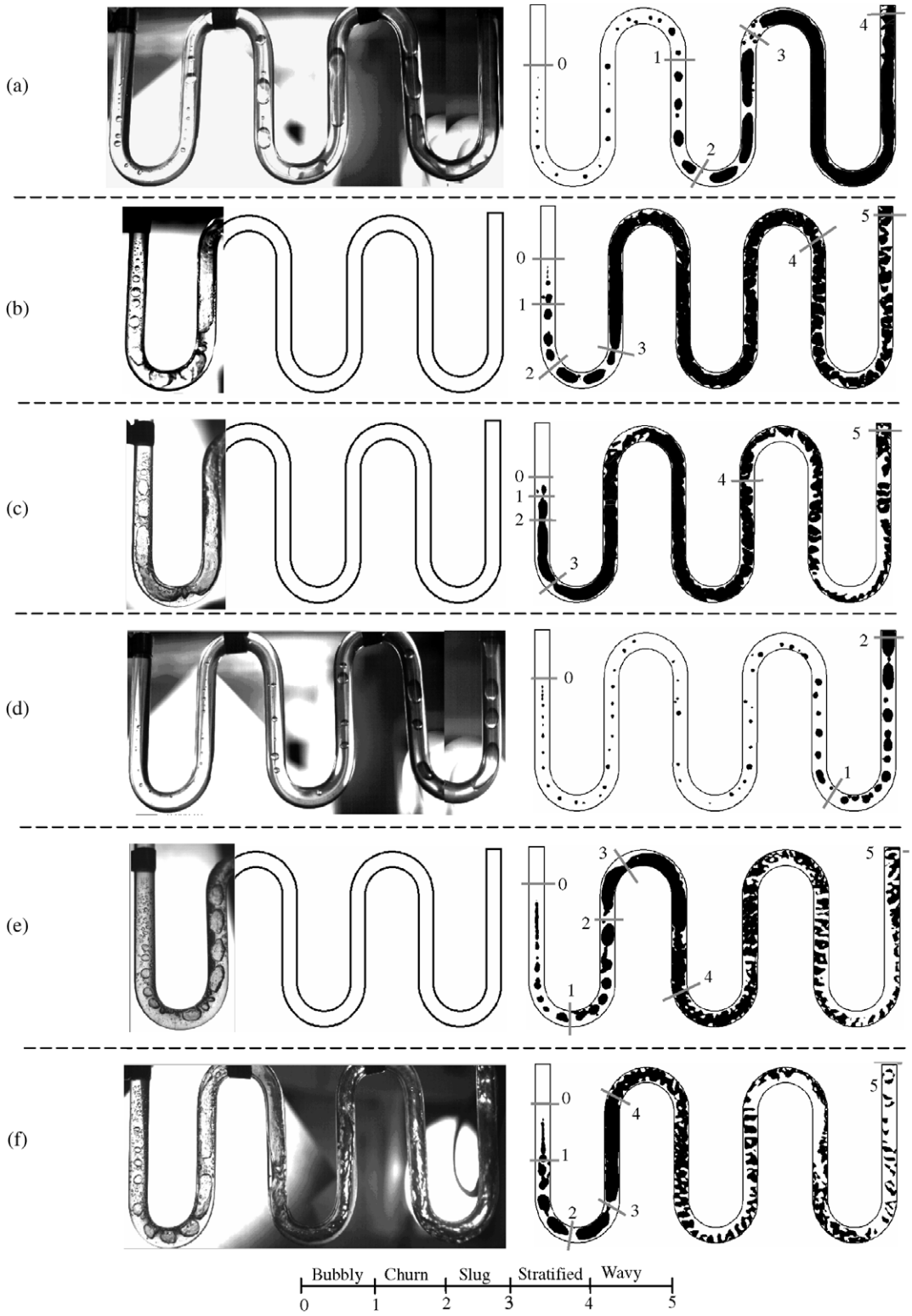

Fig. 3. Comparison between the simulations (right) and the experimental observations (left): dark areas in the simulation images are the vapor–liquid interface: (a) case 1; (b) case 2; (c) case 3; (d) case 4; (e) case 5; (f) case 6.

4.2. Flow in straight tube

Case 1(b) and (c) in Fig. 5 illustrate the simulated phase and pressure distribution on the vertical symmetric planes of the straight sections in case 1. In the first straight tube section close to the inlet, an active site is set on the bottom tube wall, just as observed in the experiments. It should be mentioned that an active site is very important to the flow

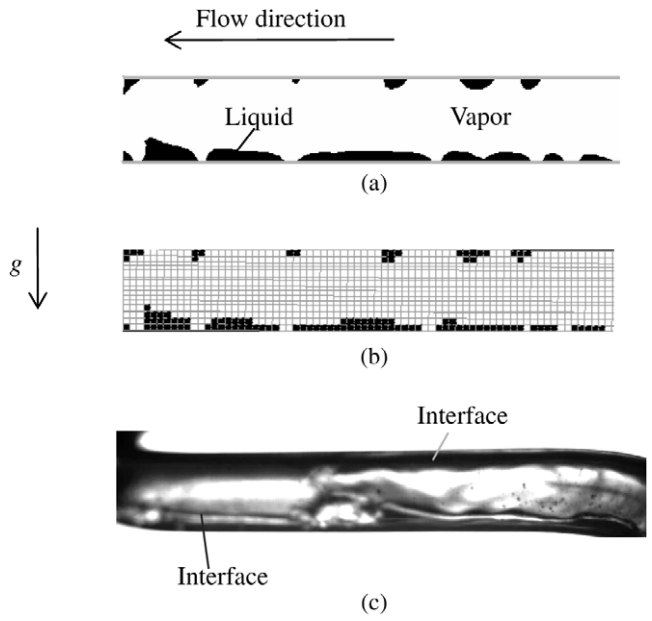

Fig. 4. Wavy thin liquid film behavior: (a) simulated thin film flow; (b) liquid occupation in grids; (c) experimental observation on the last straight tube in case 5.

pattern in the subcooled region, and simulations ignoring this factor would deviated greatly form the experimental observations. However, cases with high heat flux and low flowrate do not rely too much on active sites, because the subcooled region in these cases is small and its influence on the flow pattern is significantly reduced. Once a small vapor is formed at the active site, it flows upward and downstreamwise due to the effects of the buoyancy and flow flushing, forming a small bubble stream. These small bubbles, floating on the top of the tube, continuously grow up, and subsequently evolve into slugs. In the further downstream region, the slugs are easy to coalesce into continuous vapor region and the flow mode turns into a stratified one. The pressure appears the highest in the most upstream straight tube section and the lowest in the most downstream straight tube section. In a specified straight tube section, gravity governs the pressure distribution, the pressure generally decreasing along vertical direction, especially in cases with lower flowrate and heat flux, as shown by case 1(c) in Fig. 5. Due to the surface tension, higher pressure appears in the interior of small bubbles, as seen in the most upstream straight tube section of case 1(c) in Fig. 5. The highest velocity appears in the vapor layer of the most down-stream straight tube section, as shown in case 1(a) of Fig. 6. Apparently, the accumulated volume expansion, caused by the evaporation in the entire tube, most significantly accelerates the vapor flow near the exit. Regional velocity vectors also show two different multiphase flow modes: (1) small bubbles being carried within the liquid flow; and (2) the vapor and liquid flowing in

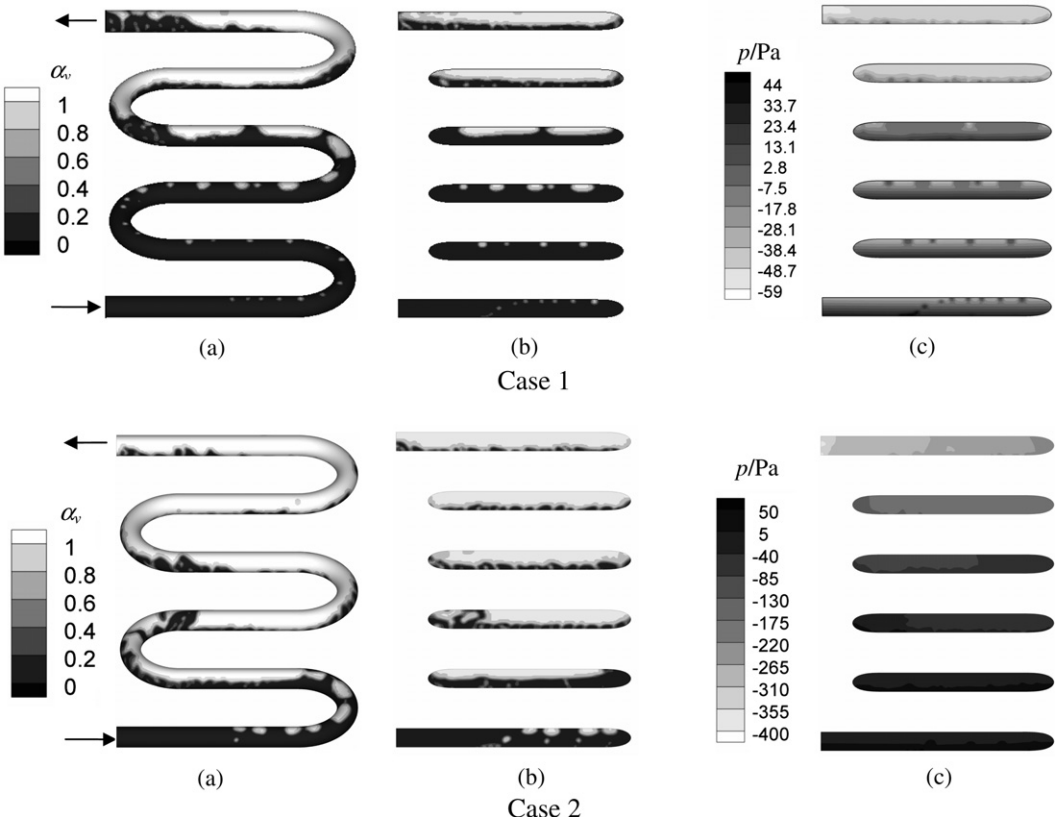

Fig. 5. Vapor volume fraction and pressure profiles in cases 1 and 2: (a) vapor volume fraction on the tube wall and (b) on the vertical symmetric planes; (c) pressure on the vertical symmetric planes.

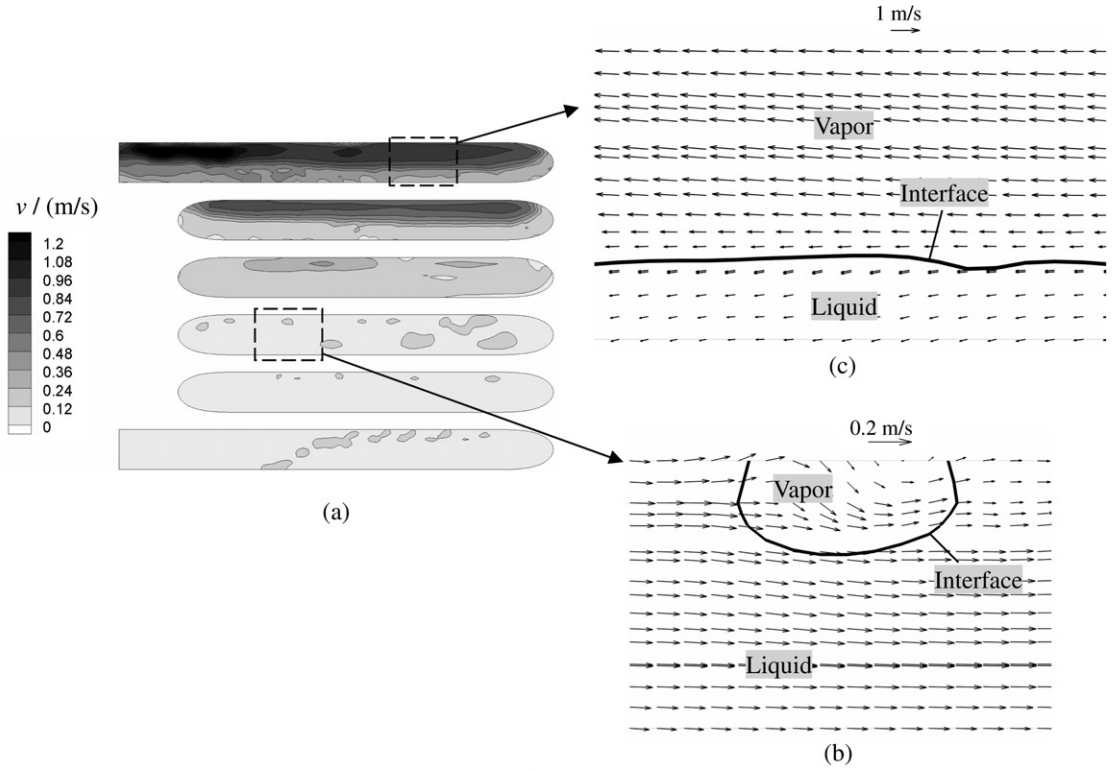

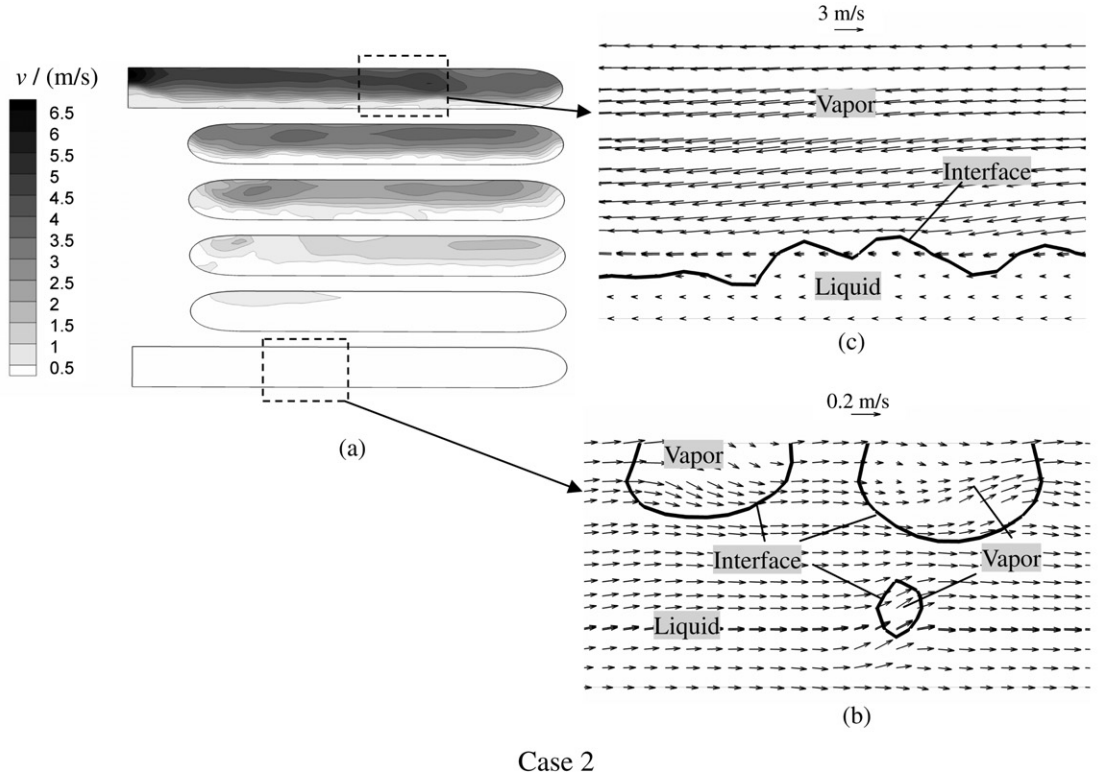

Fig. 6. Velocity profiles in cases 1 and 2: (a) velocity magnitude on vertical symmetric planes; (b and c) velocity vectors in local regions.

separate zones, corresponding to bubbly/churn flow mode and stratified flow mode, respectively. In the first mode the velocities of liquid and vapor are almost the same while in the second mode great velocity difference exists between two phases, as shown by case 1(b) and (c) in Fig. 6, respectively. In the stratified flow mode in the region close to the

exit, the continuous vapor layer is formed or, in another word, the vapor passage is opened, so the flow resistance in the vapor phase is greatly reduced due to its much smaller viscosity, resulting in larger velocity in vapor phase than in liquid phase. The above comments similarly can be applied to case 2 of Figs. 5 and 6. However, the liquid film in the downstream straight tube section in case 2 is thinner than that in case 1, and the vapor–liquid interface of the stratified flow mode is typically wavy, not as smooth as in case 1, as shown in case 2(c) of Fig. 6. Note that the heat flux in case 2 is higher, causing higher volumetric volume velocity at the exit of the tube. Higher velocity produces a drastically shearing and wavy effect on the liquid–vapor interface. Additionally, the rise of small bubbles drags the fluid upward and causes flow disturbance, as shown in case 2(b) of Fig. 6.

4.3. Flow in tube bends

Boiling flow in tube bends is quite different from that in straight tubes due to the influence of centrifugal force coupled with the buoyancy. Liquid–vapor interface may be expected to play a dominant role in pressure and velocity distributions.

Fig. 7 shows the phase distribution, pressure and secondary flow on cross-sections of five bends in cases 1 and 2, respectively. Obviously, the velocity vectors of secondary flow and pressure significantly differ from each other on different cross-sections since the acceleration of fluid induced by the volumetric expansion of evaporation changes with flow distance and significantly alters the fluid velocity. Also, the phase re-distribution induced by bend effects has great impact on the flow behavior in the bends.

As a comparison, a single liquid flow without wall heating was also shown for these two cases under the same flow conditions. Fig. 8 shows the distributions of secondary flow and pressure on bend cross-sections for R141B flowing without phase change. The comparison of Fig. 7 with Fig. 8 indicates that the phase change and phase distribution play a specially important role in the boiling two phase flow, greatly altering the flow characteristics.

The configuration and movement of liquid–vapor interface also characterize the velocity and pressure profiles. The pressure contours is sparse in the vapor phase, however dense in the liquid phase, as shown in Fig. 7. For small bubbles, the interior pressure is evidently higher than in the adjacent liquid region, as shown in the 3–3 plane of Fig. 7a. For large bubbles or continuous vapor layer, the liquid–vapor interface is easy to deform from a smooth surface due to the less important influence of the surface tension, as shown in the 4–4 plane of Fig. 7b. Waving of interface would produce a local movement normal to the interface, both in the liquid and vapor phases, as shown in the 2–2 and 4–4 planes of Fig. 7b. Due to the centrifugal force the liquid (the denser phase) inclines to flow away from the turning center of the tube bend, so the interface declines towards the turning center, as shown in the 4–4 plane in Fig. 7a. When the heating power is increased, the volumetric expansion drastically augments the velocity magnitude. Consequently, the decline of liquid–vapor interface is further accentuated due to the increased centrifugal force, as shown in the 4–4 plane in Fig. 7b.

5. Parameter characteristics

5.1. Pressure drop and vapor volume fraction at the outlet

During boiling flow, generation and coalesce of bubbles, and waving of liquid–vapor interface as well, result in great variation in the pressure drop ΔP between the inlet and outlet and the area-averaged volume fraction $\alpha_{v,out}$ at the outlet. The variations of ΔP and $\alpha_{v,out}$ closely depend on the flow mode at the outlet region (the last straight tube). There are three types of flow modes in the outlet region observed in the simulation: continuous waving, bubbly flow and vapor flow with separated liquid patches on the wall. Fig. 9 shows the simulated pressure drop and volume fraction for the first and second flow modes, and Fig. 10 depicts those of the third type. For all these flow modes, the valleys of $\alpha_{v,out}$ and ΔP profiles are well synchronized, indicating the volume fraction influences pressure drop significantly. The time interval between two neighboring valleys is about 0.3–0.4 s for continuous wavy flow, 0.05–0.1 s for bubbly flow and 0.01–0.02 s for the vapor flow with separated liquid patches on the wall. Mainly, there are two factors influencing the time interval, the morphology of the liquid–vapor interface and the flowrate. For example, time interval in the continuous wavy and bubbly flow is determined by the waving motion of the liquid–vapor interface. When the valley of the wave reaches the outlet, the volume fraction and pressure drop both drop to low values. Increasing flowrate would shorten the time interval for a wave section to pass through the exit and decrease the oscillation periods of $\alpha_{v,out}$ and ΔP. The time intervals in cases 3 and 6 are the shortest, as shown in Fig. 10 where the mean velocities are 4.12 m/s and 3.62 m/s, respectively. As a comparison, the average velocities in cases 1 and 4 are only 0.67 m/s and 0.16 m/s, respectively, so their time intervals are somewhat longer.

Fig. 11 shows the influence of heat flux on the time-averaged volume fraction $\alpha_{v,out,m}$ and the pressure drop ΔP_m. Both $\alpha_{v,out,m}$ and ΔP_m monotonically increase with the heat flux. The time-averaged vapor volume faction is always higher in the cases of 10 l/h than in the cases of 15 l/h because boiling flow occurs much more drastically with a lower liquid flowrate at the same wall heat flux. The time-averaged pressure drop of the flowrate 10 l/h is first higher than that of 15 l/h at the heat flux q'' less than about 15,000 W/m^2, and then becomes lower as the heat flux exceeds 15,000 W/m^2. This is mainly determined by the flowrate and the boiling process. For a single phase flow, the pressure drops increases with flowrate. The pressure drop is 44.14 Pa in the single liquid phase at the flowrate of 10 l/h while increases to 73.12 Pa at the flowrate of

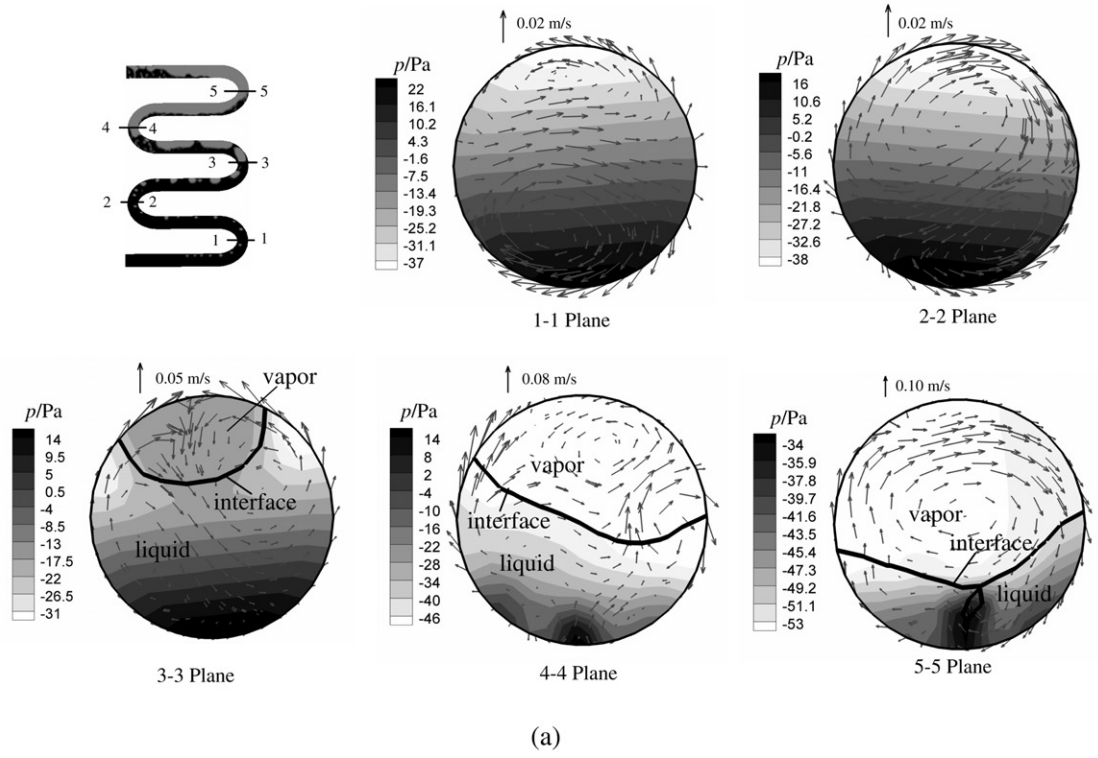

Fig. 7. Secondary flow and pressure on bend cross-sections: (a) case 1; (b) case 2.

15 l/h. Besides a higher pressure drop, the higher flowrate flow also needs a greater applied heat amount to raise its temperature to the boiling point. For the considered flowrates of 10 l/h and 15 l/h, the necessary energy required to heat the liquid to its saturation temperature right before exiting the tube via the outlet is 33.5 W and 50.3 W, corresponding to heat fluxes of 3873 W/m^2 and 5810 W/m^2, respectively. This is why the boiling process is very weak

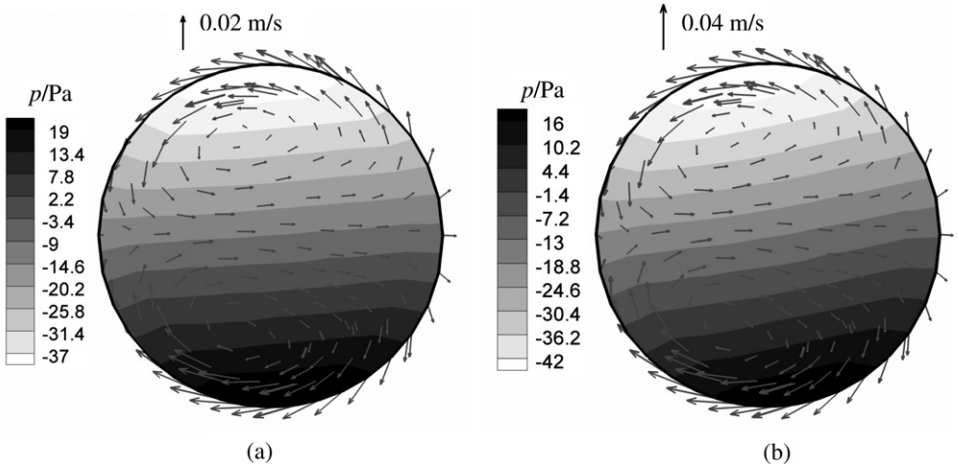

Fig. 8. Secondary flow and pressure on bend cross-sections for single phase flow: (a) 10 l/h; (b) 15 l/h.

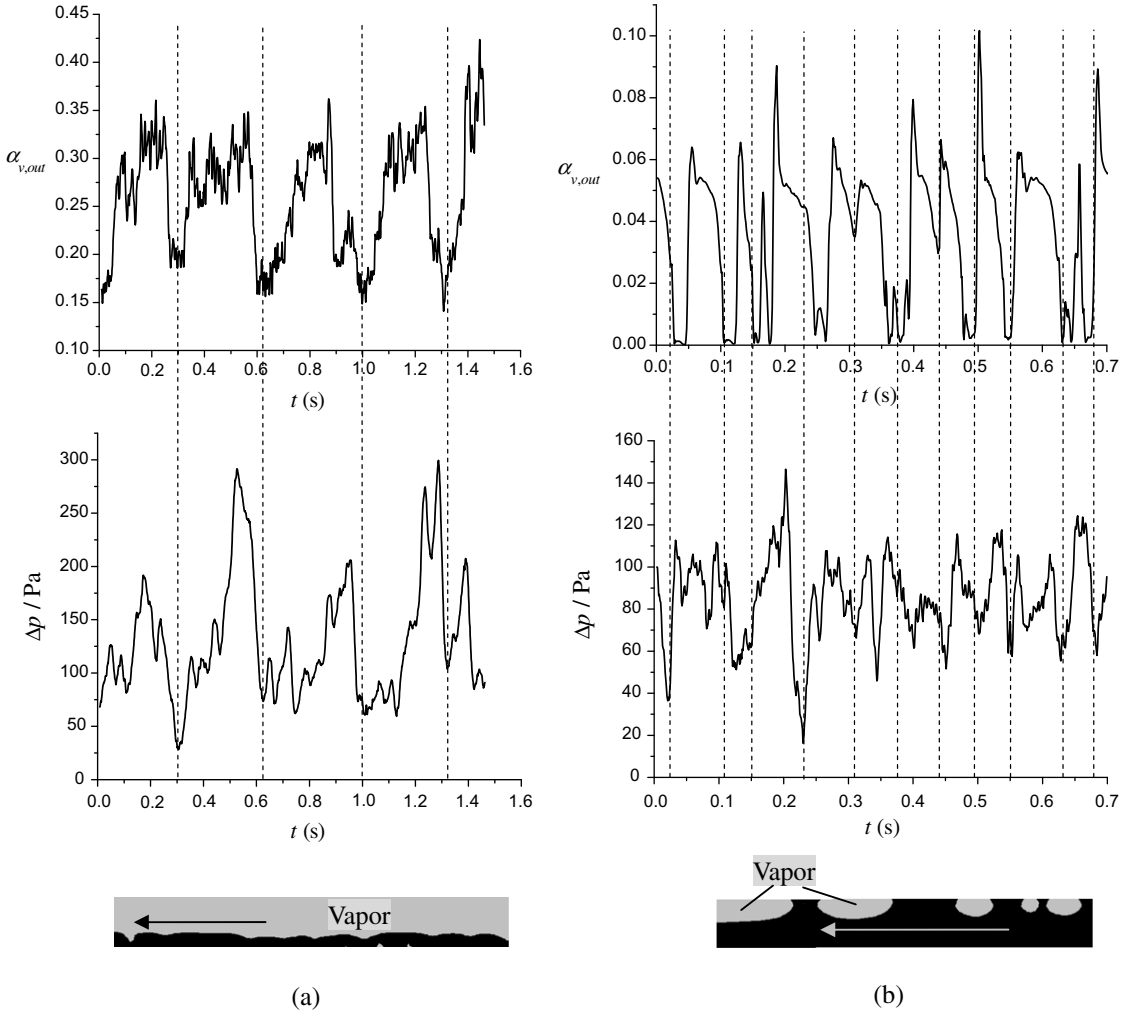

Fig. 9. Pressure drop and volume fraction at the exit for wavy and bubbly flow: (a) case 1 – wavy flow; (b) case 4 – bubbly flow.

at the heat flux of 6888 W/m^2 for the flowrate of 15 l/h with very limited boiling nucleation occurring in the tube, see Fig. 3d, while becomes relatively strong for the flowrate of 10 l/h, see Fig. 3a. Accordingly, the pressure drop is close to and obviously higher than that of the single liquid phase flow for the flowrate of 15 l/h and 10 l/h,

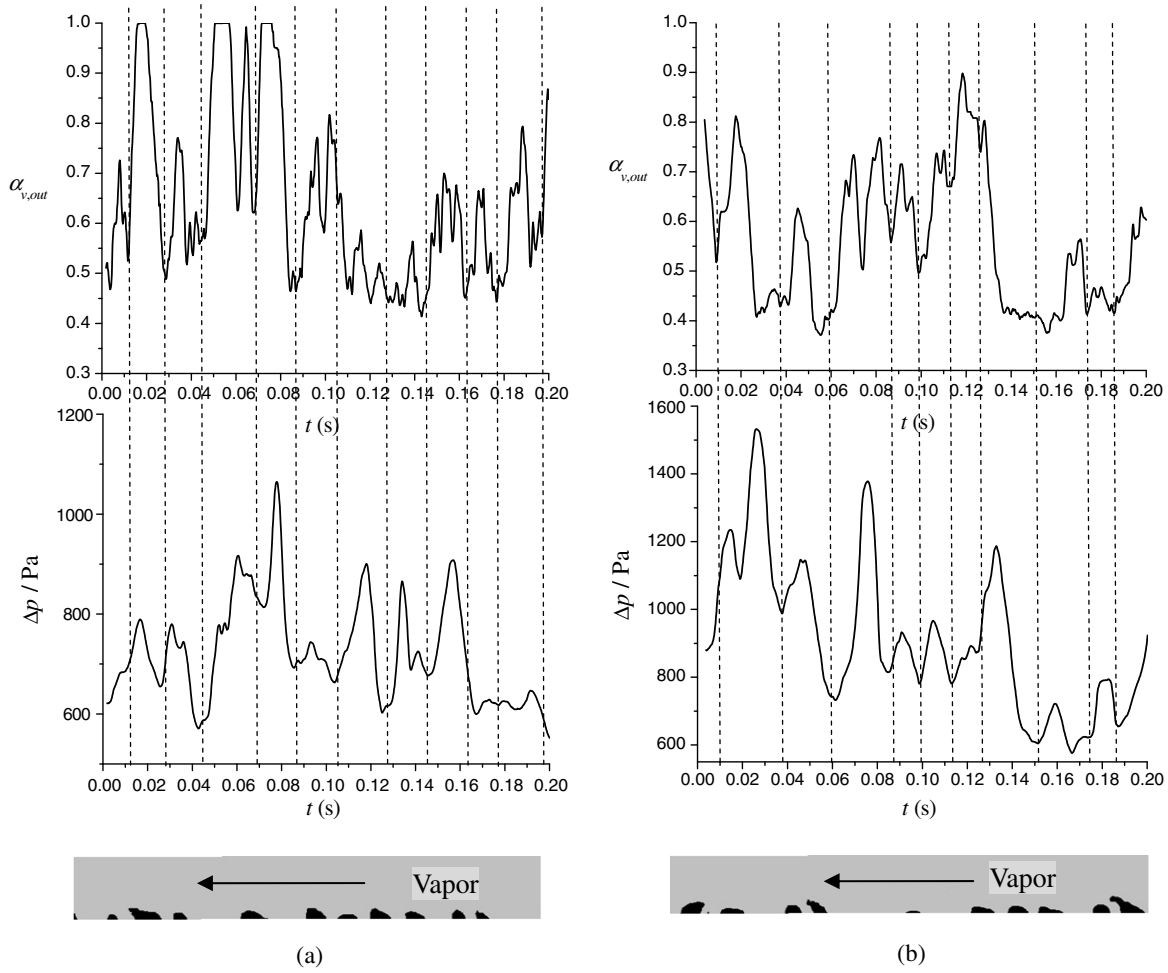

Fig. 10. Pressure drop and volume fraction at the exit for flows with liquid patches: (a) case 3; (b) case 6.

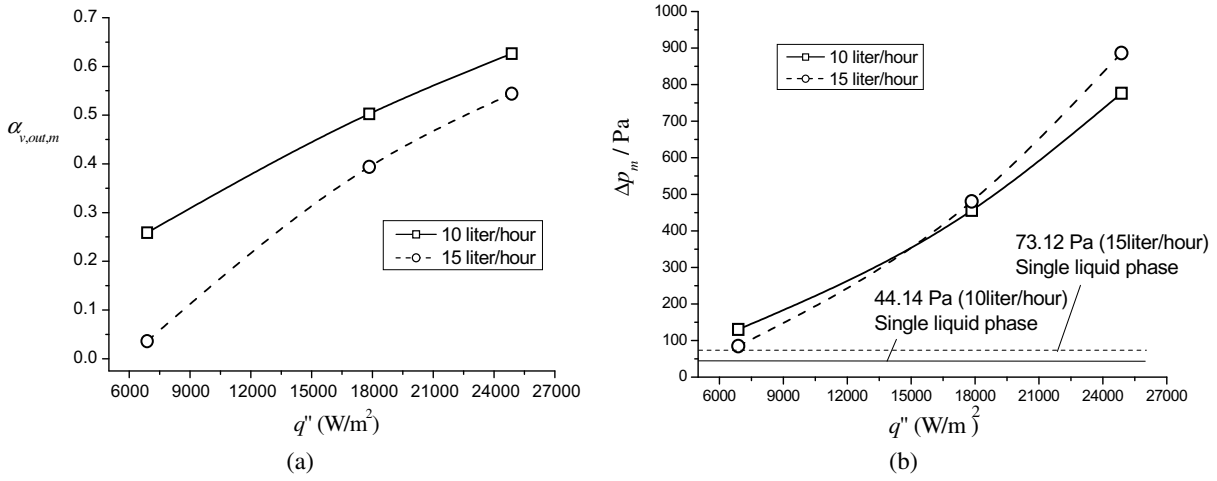

Fig. 11. Influence of wall heat flux q'': (a) time-averaged vapor volume fraction $\alpha_{v,out,m}$; (b) time-averaged pressure drop Δp_m.

respectively, see Fig. 11b. As the heat flux increases, the heat amount consumed in eliminating subcooling becomes less important in determining pressure drop, and the flowrate becomes to play more and more important role and recovers its dominant impact, as in the single liquid phase flow, on the pressure drop. Consequently, the pressure drop at the flowrate of 15 l/h exceeds that of the flowrate of 10 l/h when the heat flux surpasses 15,000 W/m^2.

5.2. Temperature behavior

As observed in all cases, the flow mode, or the phase distribution, significantly influences the temperature profile. Because of the smaller thermal conductivity and capacity in vapor phase than in liquid phase, temperature and its gradient should be much higher in vapor than in liquid. Fig. 12 shows the distributions of temperature and phases on the tube wall for two typical cases. The high temperature region corresponds well to the vapor region, especially in larger bubbles and stratified vapor regions. The hottest area in case 3 appears in the slug flow region in the first tube bend, not in the downstream region as in case 1. Although the volume fraction is much higher in the downstream region however the velocity is also larger there. So the convective heat transfer is efficient to remove the wall heat flux and keep the wall at a relatively low temperature. This is why the wall temperature in the downstream is abnormally lower than in the upstream region, as shown in case 3(a) of Fig. 12.

Fig. 13a shows the temperature details around a bubble on the tube wall area enclosed by the dashed rectangle in case 1(a) of Fig. 12. Due to the efficient evaporation cooling, the temperature on the liquid–vapor interface is well maintained at the saturation temperature 307.65 K, and the highest temperature is in the center region of the bubble. Although a great temperature gradient appears in the bubble, the temperature profile in the liquid region is fairly uniform. Fig. 13b shows the temperature distribution on the vertical plane cut along a–a line. Evidently, the temperature on the interface is maintained at the saturation temperature, and the highest temperature appears in the vapor region adjacent to the heating wall.

6. Conclusions

Numerical simulations and experiments were conducted to investigate the flow boiling of refrigerant R141B in a horizontal coiled tube. The comparison indicated that the phase distributions in various cases predicted by the

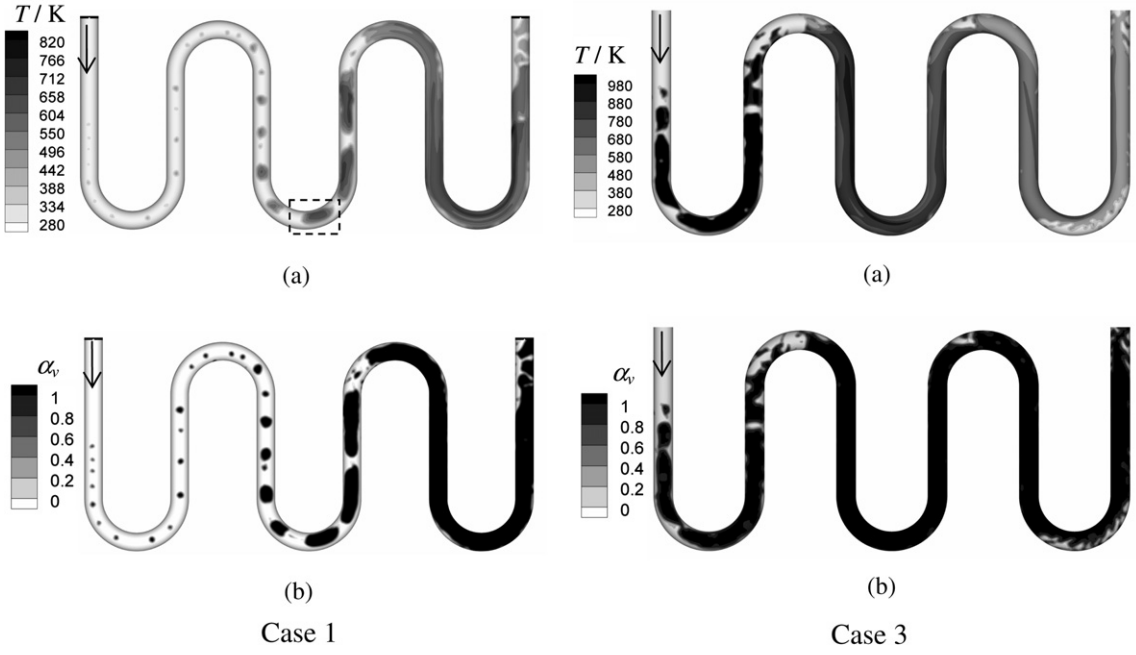

Fig. 12. Profiles on the top tube wall in cases 1 and 3: (a) temperature; (b) vapor volume fraction.

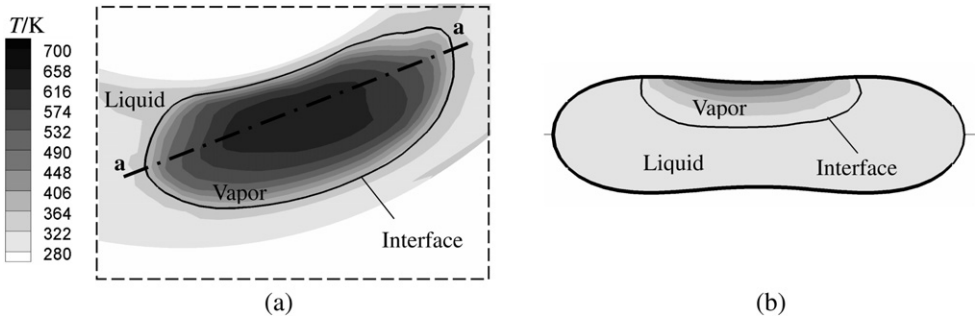

Fig. 13. Temperature around a bubble: (a) on the tube wall; (b) on the vertical plane cut along a–a line.

simulations were well consistent with those observed in the experiments. Particularly, the simulations comprehensively exhibited the evolution process of flow mode depending on hydrodynamical and thermal flow conditions.

Flow velocity predicted in the simulations showed a strongly dependence on the phase distribution. In bubbly flow vapor phase flowed with liquid phase, showing less difference of velocities between two phases, whereas in stratified flow vapor flowed much faster than liquid did and caused the phase interface to wave significantly. Special interests were addressed on the flow in the tube bends, and the study on secondary flow in these tube bends showed that liquid–vapor interface, in addition to the centrifugal force and buoyancy, played a dominant role in pressure and velocity profiles.

The variations of pressure drop and vapor volume fraction at the outlet were found in a close relation with the phase interface motion at the tube outlet. Both the morphology of the liquid–vapor interface and the flowrate had important influences on the variations of pressure drop and vapor volume fraction. Increasing wall heat flux enlarged pressure drop and vapor volume fraction at the outlet of the tube.

On the tube wall, the high temperature area corresponded to the vapor area very well and the temperature profile was very similar to the phase profile, especially in larger bubbles and stratified vapor regions. Due to the efficient heat removal of evaporation, the liquid phase was maintained at around the saturation temperature.

Acknowledgements

This work is currently supported by Specialized Research Fund for the Doctoral Program of High Education (Contract No. 20040003076) and Advanced Heat Transfer LLC, USA.

References

[1] Y. Taitel, A.E. Dukler, A model for predicating flow regime transitions in horizontal and near horizontal gas–liquid flow, Amer. Inst. Chem. Eng. (AIChE) J. 22 (2) (1976) 43–55.

[2] T.G. Theofanous, T.J. Hanratty, Report of study group on flow regimes in multifluid flow, Int. J. Multiphase Flow 29 (Appendix 1) (2003) 1061–1068.

[3] K. Hashizume, Flow pattern and void fraction of refrigerant two-phase flow in a horizontal pipe, Bull. Jpn. Soc. Mech. Eng. 26 (219) (1983) 1597–1602.

[4] D. Steiner, Heat transfer to boiling saturated liquids, in: V.D. Ingenieure (Ed.), VDI-warmeatlas (VDI Heat Atlas) (J.W. Fullarton, Trans.), VDI-Gessellschaft Verfahrenstchnik und Chemieingenieurwesen (GCV), Dusseldorf, Germany, 1993.

[5] N. Kattan, Contribution to the heat transfer analysis of substitute refrigerants in evaporator tubes with smooth and enhanced surfaces, Theses No. 1498, Swiss Federal Institute of Technology, Lausanne, 1996.

[6] N. Kattan, J.R. Thome, D. Favrat, Flow boiling in horizontal tubes: Part 1 – development of a diabatic two-phase flow pattern map, Int. J. Heat Transfer 120 (1998) 140–147.

[7] N. Kattan, J.R. Thome, D. Favrat, Flow boiling in horizontal tubes: Part 3 – development of a new heat transfer model based on flow pattern, Int. J. Heat Transfer 120 (1998) 156–165.

[8] J.R. Thome, J.E. Hajal, Two-phase flow pattern map for evaporation in horizontal tubes: latest version, in: Proceedings of the First International Conference on Heat Transfer, Fluid Mechanics and Thermodynamics, South Africa, 2002, pp. 182–188.

[9] L. Wojtan, Experimental and analytical investigation of void fraction and heat transfer during evaporation in horizontal tubes, Thesis No. 2978, Swiss Federal Institute of Technology, Lausanne, 2004.

[10] R. Scardovelli, S. Zaleski, Direct numerical simulation of free-surface and interfacial flow, Ann. Rev. Fluid Mech. 31 (1999) 567–603.

[11] T. Yabe, F. Xiao, T. Utsumi, The constrained interpolation profile (cip) method for multi-phase analysis, J. Comput. Phys. 169 (2001) 556–593.

[12] J.A. Sethian, Evolution, implement, and application of level set and fast marching methods for advancing fronts, J. Comput. Phys. 169 (2001) 503–555.

[13] S. Osher, R.P. Fedkiw, Level set methods, J. Comput. Phys. 169 (2001) 462–463.

[14] D. Jacqmin, Calculation of two-phase Navier–Stokes flows using phase-field modeling, J. Comput. Phys. 155 (1999) 96–127.

[15] G. Tryggvason, A. Esmaeeli, N. Al-Rawahi, Direct numerical simulations of flows with phase change, Comput. Struct. 83 (2005) 445–453.

[16] S.W.J. Welch, J. Wilson, A volume of fluid based method for fluid flows with phase change, J. Comput. Phys. 160 (2000) 662–682.

[17] A. Esmaeeli, G. Tryggvason, Computations of film boiling. Part I, Numerical method, Int. J. Heat Mass Transfer 47 (2004) 5451–5461.

[18] H.L. Wu, X.F. Peng, P. Ye, Y. Gong, Simulation of refrigerant flow boiling in serpentine tubes, Int. J. Heat and Mass Transfer 50 (2007) 1186–1195.

[19] M. Shur, P.R. Spalart, M. Strelets, A. Travin, Detached-eddy simulation of an airfoil at high angle of attack, in: Proceedings of the 4th International Symposium on Engineering Turbulence Modeling and Experiments, Corsica, France, May 1999.

[20] S.E. Kim, D. Choudhury, B. Patel, Computations of complex turbulent flows using the commercial code FLUENT, in: Proceedings of the ICASE/LaRC/AFOSR Symposium on Modeling Complex Turbulent Flows, Hampton, VA, 1997.

[21] W.H. Lee, A pressure iteration scheme for two-phase flow modeling, in: T.N. Veziroglu (Ed.), Multiphase Transport Fundamentals, Reactor Safety, Applications, vol. 1, Hemisphere Publishing, Washington, DC, 1980.